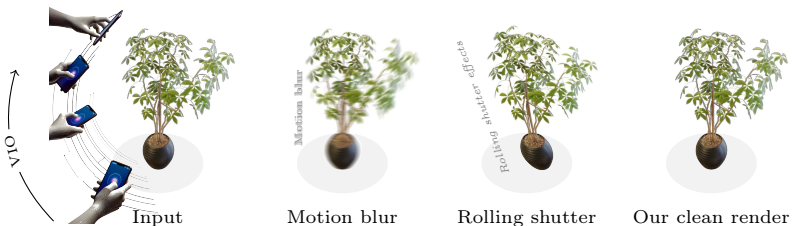


# Gaussian Splatting on the Move: Blur and Rolling Shutter Compensation for Natural Camera Motion

Otto Seiskari<sup>1</sup>, Jerry Ylilammi<sup>1</sup>, Valtteri Kaatrasalo<sup>1</sup>, Pekka Rantalankila<sup>1</sup>,  
Matias Turkulainen<sup>2</sup>, Juho Kannala<sup>1,3</sup>, Esa Rahtu<sup>1,4</sup>, and Arno Solin<sup>1,3</sup>

<sup>1</sup> Spectacular AI, <sup>2</sup> ETH Zurich, <sup>3</sup> Aalto University, <sup>4</sup> Tampere University  
Corresponding author: [otto.seiskari@spectacularai.com](mailto:otto.seiskari@spectacularai.com)

**Abstract.** High-quality scene reconstruction and novel view synthesis based on Gaussian Splatting (3DGS) typically require steady, high-quality photographs, often impractical to capture with handheld cameras. We present a method that adapts to camera motion and allows high-quality scene reconstruction with handheld video data suffering from motion blur and rolling shutter distortion. Our approach is based on detailed modelling of the physical image formation process and utilizes velocities estimated using visual-inertial odometry (VIO). Camera poses are considered non-static during the exposure time of a single image frame and camera poses are further optimized in the reconstruction process. We formulate a differentiable rendering pipeline that leverages screen space approximation to efficiently incorporate rolling-shutter and motion blur effects into the 3DGS framework. Our results with both synthetic and real data demonstrate superior performance in mitigating camera motion over existing methods, thereby advancing 3DGS in naturalistic settings.



## 1 Introduction

The field of novel view synthesis has seen significant advancements in recent years, with the introduction of Neural Radiance Fields (NeRF, [27]) and more recently, Gaussian Splatting (3DGS, [13]). Both classes of methods represent scenes as differentiable, non-mesh-based, 3D representations that allow rendering of new views that are often visually indistinguishable from evaluation images. One major limitation of these methods is that they generally require high-quality still photographs which can be accurately registered using photogrammetry software, such as COLMAP [32].

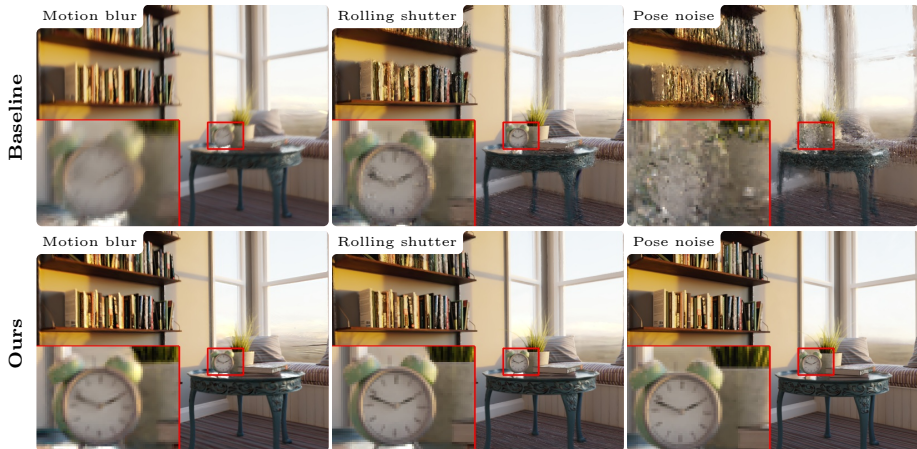


**Fig. 1:** 3DGS reconstructions from the synthetic *cozyroom* scene under different simulated effects with (bottom row) and without (top row) our compensation. The corresponding numerical results are given in Table 1. The bottom right image is visually indistinguishable from the reference (PSNR 35.9).

Generating 3D reconstructions from casually captured data recorded with a moving hand-held camera, such as a smartphone, would enable faster data collection and integration into a broader range of use cases. However, image data from a moving sensor is prone to motion blur and rolling shutter distortion, which significantly degrade the quality of the reconstruction and increases the likelihood of failures in pose registration. Motion blur effects occur during the camera shutter’s opening time due to relative motion between the camera and objects in the scene. Similarly, rolling shutter effects, caused by the camera sensor scanning the scene line-by-line, lead to warping distortions in fast-moving scenes or during rapid camera maneuvers.

Most of the existing methods aiming to compensate for these effects use classical or deep learning–based approaches to recover sharpened versions of the input images, without the aid of an underlying 3D image formation model for the scene. The recent 3D novel view synthesis methods, including NeRF [27] and 3DGS [13], allow for an alternative approach where a sharp 3D reconstruction is recovered without manipulating the training image data as an intermediary step. Deblur-NeRF [25], and BAD-NeRF [41] perform this in the context of NeRFs and [17] in the context of 3DGS.

This work offers an alternative deblurring and rolling shutter correction approach for the 3DGS framework. Instead of learning blurring kernels from the data, as in [25], we directly model the image formation process with camera motion and rolling shutter effects leveraging velocity estimates computed using visual-inertial odometry (VIO), a technique that fuses inertial measurement unit (IMU) data with monocular video.



**Fig. 2:** Further 3DGS reconstructions from the synthetic `factory` scene. The Splatfacto method acting as a baseline. The corresponding numerical results are given in Table 1.

We formulate an efficient differentiable motion blur and rolling-shutter capable rendering pipeline that utilizes screen space approximation to avoid recomputing or hindering the performance of 3DGS operations. To address the ill-posed nature of the de-blurring problem (*cf.* [11]), we leverage the regularization capabilities of the differentiable 3DGS framework and further add regularization and priors from sensor data to reduce artefacts and increase the quality of the results (see Fig. 1 for examples).

The performance of our method is evaluated using both synthetic data from the Deblur-Nerf data set [25] as well as real-world data recorded using mobile devices. Our method is implemented as an extension to the NerfStudio [39] and `gsplat` [47] software packages, which serve as our baseline methods for evaluation. Our approach consistently outperforms the baselines for both synthetic and real data experiments in terms of PSNR, SSIM, and LPIPS metrics, and the resulting reconstructions appear qualitatively sharper.

## 2 Related Work

We cover classical and deep learning-based image deblurring and give an overview of prior methods compensating for motion blur and rolling shutter distortion in the context of 3D reconstruction using implicit representations.

**Image deblurring** Motion blur compensation has been extensively studied in single and multi-image settings. Classical approaches attempt to jointly recover sharp input images along with blurring kernels with optimization based methods [31, 37]. This task is ill-posed since multiple blurring kernels can result in the same blurred image, and prior work add regularization to account for this [2, 35, 44]. Richardson–Lucy deblurring [38] attempts to account for spatially

varying blurring with projective homographies to describe three-dimensional camera motion. Deep learning-based methods (*e.g.*, [3, 8, 15]) utilize features learned on large training data sets to recover sharp images. These methods outperform classical approaches that rely on hand crafted image statistics and can better handle spatially varying deblurring.

Similarly, rolling shutter (RS) compensation has been traditionally studied as a problem of optimally warping individual pixels or images to account for the row-wise exposure of frames [9, 16, 19, 30]. Modern methods such as [6, 22, 40] utilize information from three-dimensional image formation and camera motion to better compensate for RS effects. Moreover, deep-learning based methods trained on large data sets demonstrate occlusion and in-painting capability, a feature that traditional methods lack. Rolling-shutter compensation has also been studied in the scope of Structure-from-Motion (SfM) and Visual-Inertial SLAM methods [10, 20, 23, 33].

Simultaneous motion blur and rolling shutter compensation has also been studied, in, *e.g.*, [28, 36]. Learning-based methods aimed at generic image blur and artefacts, such as [48], have also improved significantly and were used in [25] as a pre-processing step to enhance NeRF reconstruction.

**Deblurring 3D implicit representations** Deblurring differentiable implicit representations for novel view synthesis is a relatively new topic and has been previously studied in [5, 25, 41] for NeRF [27] representations and [17] in the 3DGS [13] context. Both [25] and [17] incorporate additional learnable parameters that model blurring effects as part of the rendering pipeline in the form of small Multi-Layer Perceptrons (MLPs) added to the baseline models. These methods treat the training images as fixed in time and focus on extracting sharper images from blurred inputs. An alternative method is to model the per frame image formation model by accounting for the motion trajectory during the capture process as presented in [41]. Our approach is most similar to [41] in the sense that we explicitly model the blur formation process by integrating information over a short camera trajectory. Rolling shutter effects, which are not considered in the aforementioned works, is separately considered in the NeRF context in [18], which also incorporates additional learnable parameters to the training process. In contrast, our approach does not include any additional trainable parameters nor MLPs to the 3DGS pipeline, and instead uses information readily available from IMU data captured from Visual-Inertial Odometry (VIO) pipelines.

Our method also utilizes pose optimization in the 3DGS framework, primarily for better pose registration in the presence of rolling shutter effects, which are not efficiently handled by COLMAP [32]. Pose refinement can also contribute to sharpening the reconstruction quality by effectively mitigating deblurring caused by the sensitivity of NeRF and 3DGS based methods on accurate pose estimates. Pose refinement has been previously applied to 3DGS in [7, 12, 26, 45], but not together with rolling shutter compensation. Correspondingly, pose optimization with NeRFs has been studied in several works (*e.g.*, [29, 41]), starting with BARF [21]. Utilizing information from VIO in NeRFs to stabilize pose optimiza-

tion has been studied in [14], but to the best of our knowledge, has not been studied in the 3DGS context.

Our implementation is based on Nerfstudio [39] and `gsplat` [47]. For robust VIO, we utilize the Spectacular AI SDK, a proprietary VISLAM system loosely based on [34].

### 3 Methods

We start with setting notation through an overview of Gaussian Splatting as a foundation for differentiable rendering, followed by our novel method of modelling motion blur and rolling shutter effects as camera motion. For this, we also introduce screen space approximation and pixel velocity-based rasterization, concluding with the regularization strategies employed to refine our results.

#### 3.1 Gaussian Splatting

Gaussian Splatting (3DGS, [13]) serves as an example and current cornerstone of *differentiable rendering*, enabling the differentiation of a pixel’s colour in relation to model parameters. This capability allows for the optimization of a loss function by comparing synthetic images to real reference images. In essence, Gaussian Splatting maps the 3D scene into 2D images through a series of Gaussian distributions, each representing a point in the scene with specific attributes such as position, shape, transparency, and colour.

In Gaussian Splatting, the colour

$$C_i(x, y, P_i, \mathcal{G}) \in \mathcal{C} \quad (1)$$

of the pixel  $(x, y) \in [0, W) \times [0, H)$  of output image  $i$  can be differentiated with respect to the model parameters  $\mathcal{G}$ , and these parameters can be used to optimize a loss function

$$\mathcal{G} \mapsto \sum_{i=1}^{N_{\text{img}}} \mathcal{L}[C_i(\cdot, \cdot, P_i, \mathcal{G}), C'_i] \quad (2)$$

comparing the synthetic images  $C_i$  to a set of  $N_{\text{img}}$  real reference images  $C'_i$ . We denote by  $P_i \in \text{SE}(3)$  camera pose corresponding to image  $i$  and assume  $\mathcal{C} = \mathbb{R}^3$  for RGB colours.

The 3DGS model parameters consist of a set

$$\mathcal{G} = \{(\mu_j, \Sigma_j, \alpha_j, \theta_j)\}_j$$

of Gaussian distributions  $(\mu_j, \Sigma_j)$ , transparencies  $\alpha_j$  and view-dependent colours  $\theta_j \in \mathcal{C}^{N_{\text{sh}}}$  represented by  $N_{\text{sh}}$  spherical harmonic coefficient vectors.

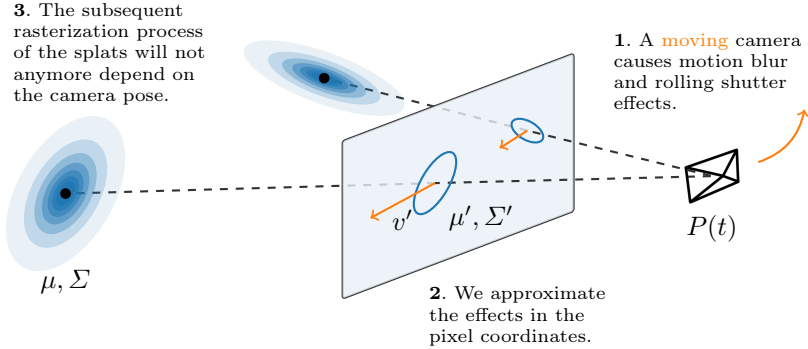


**Fig. 3:** Screen space approximation incorporates the motion during the frame exposure interval into our model by capturing its effect in pixel coordinates in the image plane. In our approach, the rendering model of 3DGS is decomposed into two stages: first, transforming the Gaussian parameters from world to pixel coordinates, and then rasterizing these parameters onto the image.

### 3.2 Blur and Rolling Shutter as Camera Motion

We simultaneously model motion blur and rolling shutter as dynamic three-dimensional effects caused by the motion of the camera along a continuous trajectory  $t \mapsto P(t)$ . In terms of 3DGS, this can be modelled by changing the rendering equation to

$$C_i(x, y, \mathcal{G}) = g \left( \frac{1}{T_e} \int_{-\frac{1}{2}T_e}^{\frac{1}{2}T_e} C_i(x, y, P(t_i + t_e + (y/H - 1/2)T_{ro}), \mathcal{G}) dt_e \right), \quad (3)$$

where  $T_{ro}$  is the rolling-shutter readout time,  $T_e$  the exposure time, and  $t_i$  the frame midpoint timestamp. Following [25], we assume a simple gamma correction model:  $g(R, G, B) = (R^{1/\gamma}, G^{1/\gamma}, B^{1/\gamma})$  with  $\gamma = 2.2$ . As a result, the colors  $\theta_j$  of the splats are defined in *linear RGB* space, whereas the original version (Eq. (1)) models them directly in the gamma-corrected colour space.

We model the camera motion around the frame midpoint time  $t_i$  as

$$P(t_i + \Delta t) = [R | p](t) = [R_i \exp(\Delta t[\omega_i]_{\times}) | p_i + \Delta t \cdot R_i v_i], \quad (4)$$

where  $(v_i, \omega_i)$  are the linear and angular velocities of the camera in its local coordinate system (assumed constant throughout the frame interval  $|\Delta t| < \frac{1}{2}(T_e + T_{ro})$ ).

### 3.3 Screen Space Approximation

In our approach, the rendering model of 3DGS is decomposed into two stages: first, transforming the Gaussian parameters from world to pixel coordinates, and then rasterizing these parameters onto the image. This transformation is pivotal

for incorporating motion effects due to camera movement during frame capture. By approximating the motion in pixel coordinates, we focus on adjusting the Gaussian means to reflect this movement, simplifying the model by primarily altering these means while keeping other parameters stable. An informal sketch of this process is visualized in Fig. 3.

These two main phases in the 3DGS rendering model can be written as  $C_i(x, y, \mathcal{G}, P_i) = r(x, y, p(\mathcal{G}, P_i))$ , where  $p$  maps the Gaussian parameters  $\mathcal{G}$  defined in world coordinates to parameters  $\{\mathcal{G}'_{i,j} = (\mu'_{i,j}, d_{i,j}, \Sigma'_{i,j}, \alpha_j, c_{i,j})\}$  defined in pixel coordinates of the currently processed camera  $i$  and individual Gaussian  $j$  (see App. A.2 for details). The subsequent rasterization phase  $r$  does not depend on the camera pose  $P_i$ .

We incorporate camera motion during the frame exposure interval into our model by approximating its effect in pixel coordinates as

$$\mu'_{i,j}(\Delta t) \approx \tilde{\mu}_{i,j}(\Delta t) := \mu'_{i,j}(0, 0) + \Delta t \cdot v'_{i,j} \quad (5)$$

in particular, we neglect the effect of (small) camera motion on the other view-dependent intermediary variables ( $d_{i,j}, \Sigma'_{i,j}, c_{i,j}$ ) and only model the effect on the pixel coordinates  $\mu'_{i,j}$  of the Gaussian means and introduce a new set of variables, the *pixel velocities* computed as

$$v'_{i,j} = -J_i(\omega_i \times \hat{\mu}_{i,j} + v_i), \quad (6)$$

where  $J_i = \text{diag}(f_x, f_y)/d_{i,j}$  is the Jacobian of the projective transform as in [13] (see App. A.4 for details).

### 3.4 Rasterization with Pixel Velocities

We approximate the integral in Eq. (3) with a sum of  $N_{\text{blur}}$  samples on a fixed uniform grid during the exposure interval

$$\tilde{C}_i(x, y, \mathcal{G}) := g \left( \frac{1}{N_{\text{blur}}} \sum_{k=1}^{N_{\text{blur}}} \tilde{C}_i(x, y, \mathcal{G}, \Delta t_k(y)) \right), \quad (7)$$

where

$$\Delta t_k(y) := \left( \frac{k-1}{N_{\text{blur}}-1} - \frac{1}{2} \right) \cdot T_e + \left( \frac{y}{H} - \frac{1}{2} \right) \cdot T_{\text{ro}}. \quad (8)$$

The 3DGS alpha blending stage (*cf.* [13]) can be written as the sum  $C(x, y, \mathcal{G}) = \sum_j T_j c_{i,j} \alpha_{i,j}(\mu'_{i,j})$  over the depth-sorted Gaussians, where  $T_j = \prod_{l=1}^{j-1} (1 - \alpha_{i,l}(\mu'_{i,l}))$  is the accumulated transmittance. The dependency on other Gaussian pixel space parameters  $\mathcal{G}'_{i,j}$  other than  $\mu'_{i,j}$  has been omitted as explained in Sec. 3.3. With this, Eq. (7) becomes

$$\tilde{C}_i(x, y, \mathcal{G}) := g \left( \frac{1}{N_{\text{blur}}} \sum_{k=1}^{N_{\text{blur}}} \sum_j T_j c_{i,j} \alpha_{i,j}(\tilde{\mu}'_{i,j}(\Delta t_k(y))) \right). \quad (9)$$

Approximating camera velocity on the Gaussian means in pixel-space has the benefit that the projective transform of the 3DGS pipeline does not need to be repeated to generate each blur sample, making the method faster than treating Gaussian velocities in world space.

### 3.5 Pose Optimization

We approximate the gradient with respect to camera pose components as

$$\frac{\partial C_i}{\partial p_i} \approx - \sum_j \frac{\partial C_i}{\partial \mu_j} \quad \text{and} \quad \frac{\partial C_i}{\partial \nu} \approx - \sum_j \frac{\partial C_i}{\partial \mu_j} \frac{\partial R_i}{\partial \nu} R_i^\top (\mu_j - p_i), \quad (10)$$

where  $\nu$  is any component of  $R_i$  or a parameter it depends on. This neglects the effect of small camera motions on view-dependent colours and Gaussian precisions  $\Sigma'_{i,j}$  defined in pixel coordinates, but allows approximating the expression in terms of the Gaussian position derivatives  $\frac{\partial C_i}{\partial \mu_{j,k}}$ , which are readily available in the 3DGS pipeline. This approach is similar to [45] and derived in more detail in App. A.3.

### 3.6 Regularization

We investigate two additional regularization methods in the 3DGS training procedure to make our approach more robust: (i) Underestimating exposure time:  $\tilde{T}_e = T_e(1 - \lambda)$  (applied to synthetic and real data); (ii) Adding a different noise vector  $\eta_j^{(k)} \sim \mathcal{N}(0, (\beta|v_j|)^2 I)$  to the estimated linear velocities  $v_j^{(k)} = v_j + \eta_j^{(k)}$  on each iteration  $k$  (real data only). An alternative approach to velocity regularization could be optimizing the velocity vectors as a part of 3DGS problem. This is left for future work.

## 4 Experiments

We evaluate the performance of our method on two different data sets: synthetic data based on the Deblur-NeRF data set [25] and real data recorded using mobile phones. We implemented our method as an extension to the open source 3DGS implementation *Splatfacto* in Nerfstudio [39], which is based on *gsplat* [47]. In particular, the implementation is based on *Splatfacto* in Nerfstudio version 1.0.2 and *gsplat* version 0.1.8 (see <https://github.com/nerfstudio-project/nerfstudio/releases/tag/v1.0.2>).

### 4.1 Synthetic Data

3DGS uses a SfM-based sparse point cloud as seed points for the initialization of the Gaussian means and scales, which is typically obtained from COLMAP [32]. However, with significantly blurry and other otherwise noisy data, COLMAP



**Table 1:** Synthetic data results comparing the baseline Splatfacto method to our approach with the appropriate compensation for each variation.

	COZYROOM			FACTORY			POOL			TANABATA		
	PSNR↑	SSIM↑	LPIPS↓	PSNR↑	SSIM↑	LPIPS↓	PSNR↑	SSIM↑	LPIPS↓	PSNR↑	SSIM↑	LPIPS↓
<i>MOTION BLUR</i>												
BASILINE	26.65	.832	.196	21.76	.628	.365	32.10	.924	.075	20.44	.690	.328
OURS	<b>29.33</b>	<b>.903</b>	<b>.073</b>	<b>27.74</b>	<b>.900</b>	<b>.125</b>	<b>32.28</b>	<b>.927</b>	<b>.063</b>	<b>23.56</b>	<b>.815</b>	<b>.175</b>
<i>ROLLING SHUTTER EFFECT</i>												
BASILINE	19.40	.634	.209	15.40	.339	.340	26.87	.760	.107	13.57	.358	.427
OURS	<b>22.79</b>	<b>.780</b>	<b>.063</b>	<b>26.72</b>	<b>.884</b>	<b>.057</b>	<b>30.98</b>	<b>.903</b>	<b>.072</b>	<b>16.61</b>	<b>.525</b>	<b>.212</b>
<i>POSE NOISE</i>												
BASILINE	17.11	.500	.371	15.31	.265	.430	21.17	.479	.372	14.35	.290	.467
OURS	<b>35.92</b>	<b>.977</b>	<b>.015</b>	<b>29.01</b>	<b>.966</b>	<b>.019</b>	<b>31.57</b>	<b>.919</b>	<b>.069</b>	<b>31.93</b>	<b>.970</b>	<b>.014</b>

often fails which prevents us from obtaining good SfM estimates for initialization on synthetic data sets like Deblur-NeRF. To overcome this, we compute an initial point cloud using SIFT [24] feature matching and triangulation with the known ground truth poses from the synthetic data set, bypassing camera pose estimation from COLMAP.

We generate multiple variants of the Deblur-NeRF data set to simulate motion blur, rolling shutter, and noisy pose effects respectively. In order to obtain synthetic velocity data and simulated rolling shutter effects, we had to re-render synthetic images from the Deblur-NeRF data set [25], see App. B.1 for further details. We experiment on the following synthetic data set variants: (i) a motion blur variant, which closely matches the motion blur variant of the original Deblur-NeRF data set, (ii) a rolling shutter only variant, (iii) and a translational and angular pose noise variant, without RS or motion blur effects. In the motion blur and rolling shutter variants, we use the synthetic ground truth velocities ( $v_j, \omega_j$ ) without additional pose noise.

As in [25], the evaluation images in the data set are always rendered without blur or rollings shutter effects, which allows us to assess the novel-view synthesis performance of the underlying ‘sharp’ reconstruction independent of the accuracy of our simulation and compensation for these effects.

We train 3DGS models for 30k iterations for all of the above synthetic data sets using 3DGS Splatfacto method as our baseline and we compare novel-view synthesis metrics with our method with the appropriate compensation mode enabled (*i.e.*, rolling shutter compensation but no motion blur compensation or pose optimization for RS case). The results are shown in Table 1 and qualitatively visualized in Figs. 1 and 2. Our method consistently outperforms the 3DGS baseline across all scenarios, indicating the effectiveness of our approach in compensating for blurring and RS effects arising from camera motion in pixel space.

## 4.2 Smartphone Data

To the end of real data evaluation, we use a new data set recorded using three different smartphones: Samsung S20 FE, Google Pixel 5 and iPhone 15 Pro. The

**Table 2:** Real data results. *RS pose opt* means 2-pass 3DGS pose optimization with rolling shutter compensation. This is compared to COLMAP baseline, both with ('+ blur') and without motion blur compensation.

	COLMAP BASELINE			COLMAP + BLUR			RS POSE OPT + BLUR		
	PSNR↑	SSIM↑	LPIPS↓	PSNR↑	SSIM↑	LPIPS↓	PSNR↑	SSIM↑	LPIPS↓
IPHONE-LEGO1	28.04	.900	.169	<b>28.61</b>	<b>.918</b>	<b>.128</b>	26.40	.869	.164
IPHONE-LEGO2	27.67	.912	.133	<b>28.38</b>	<b>.921</b>	<b>.120</b>	24.73	.853	.195
IPHONE-LEGO3	25.16	.795	.261	<b>25.42</b>	<b>.817</b>	<b>.210</b>	22.93	.720	.282
IPHONE-POTS1	28.21	.896	.184	<b>28.29</b>	<b>.903</b>	<b>.158</b>	27.50	.876	.169
IPHONE-POTS2	27.16	.840	.268	<b>27.51</b>	<b>.867</b>	<b>.203</b>	26.32	.821	.234
PIXEL5-LAMP	27.21	.784	.316	26.91	.783	.317	<b>30.09</b>	<b>.820</b>	<b>.258</b>
PIXEL5-PLANT	26.30	.902	.261	26.47	.903	.243	<b>27.32</b>	<b>.908</b>	<b>.242</b>
PIXEL5-TABLE	28.70	.881	.310	28.88	.883	.296	<b>31.01</b>	<b>.884</b>	<b>.278</b>
S20-BIKE	26.66	.885	.270	26.68	.885	.272	<b>28.18</b>	<b>.894</b>	<b>.262</b>
S20-BIKERACK	25.71	<b>.800</b>	<b>.281</b>	25.65	.800	.284	<b>26.68</b>	.797	.297
S20-SIGN	23.42	.732	.280	24.07	.750	.272	<b>25.89</b>	<b>.780</b>	<b>.259</b>
AVERAGE	26.75	.848	.249	26.99	<b>.857</b>	<b>.228</b>	<b>27.00</b>	.838	.240

first two are Android phones with a known, and relatively large rolling-shutter readout time  $T_{ro}$ .

The data set consists of 11 short handheld recordings of various scenes collected using the Spectacular Rec application [1], which records synchronized IMU and video data, together with the built-in (factory) calibration information from each device. The same application is available both for Android and iOS, and it was used to capture the raw image and IMU data on the devices.

**Manual calibration** In addition to the main sequences, we recorded separate manual camera calibration data for the Android devices, using the same fixed focus distance as in the other sequences, and used the Kalibr software package (<https://github.com/ethz-asl/kalibr>) to compute a accurate intrinsic calibration parameters for those devices.

**Preprocessing and VIO velocity estimation** We first process the recorded data with the Spectacular AI SDK [1], to obtain the following: (i) A sparse set of key frames with minimum distance of 10 cm, selected to approximately minimize motion blur among the set of candidate key frames (see App. A.5 for details). (ii) For each key frame, the frame velocities  $(v_j, \omega_j)$ , based on the fusion of IMU and video data. (iii) Approximate VISLAM-based poses  $P_j^{SAI}$ .

**Training and evaluation split** As with the synthetic data and in [25], we aim to select the least blurry frames for evaluation, which is performed by splitting the (ordered) key frames to subsets of eight consecutive key frames, and for each subset, picking the least blurry one for evaluation. We use the same motion blur metric as for key frame selection in App. A.5.

**Pose estimation** After preprocessing, the poses of the key frames and camera intrinsics are estimated using COLMAP [32] (through Nerfstudio). In our main results, we only included sequences in which COLMAP did not fail due to excessively difficult visual conditions.

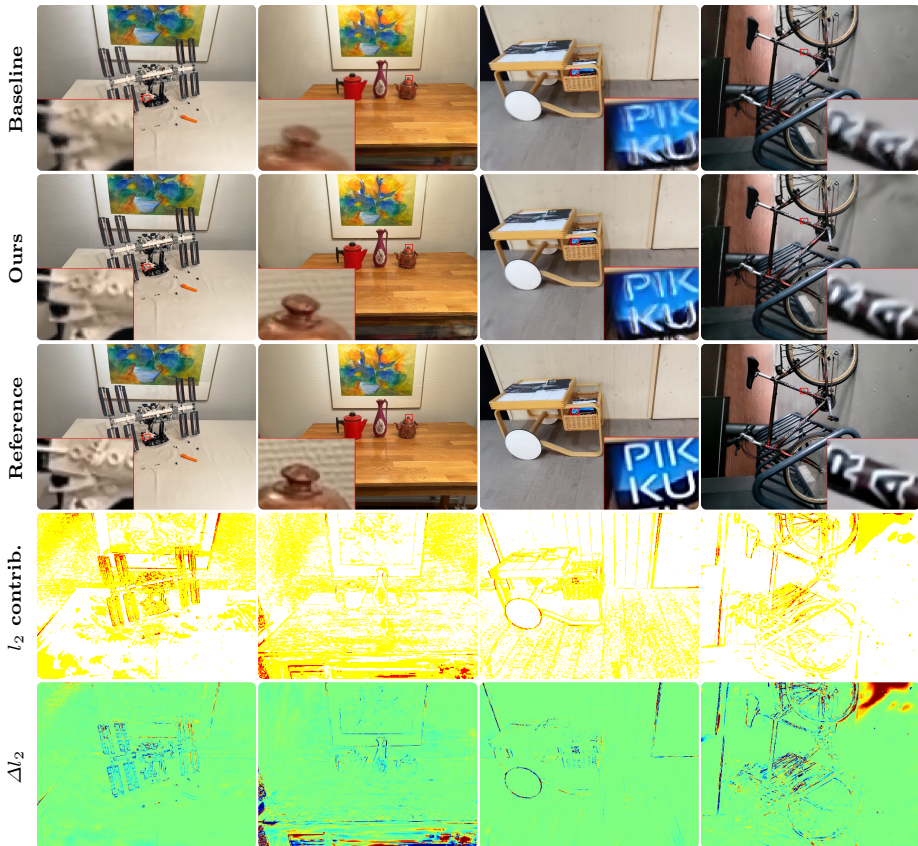


**Fig. 4:** Real data examples with scenes captured with smartphones. From top to bottom: Using COLMAP poses without motion blur compensation (baseline); with motion blur compensation (ours); reference evaluation image;  $l_2$  error contributions, ours (red: 30%, yellow: 60%, white: 10%);  $l_2$  error differences ours vs baseline (red: more error, blue: less error). Scenes: `lego1` (iPhone), `pots2` (iPhone), `table` (Pixel), `bike` (S20).

**COLMAP baseline** Our baseline comparison involves the Splatfacto method paired with poses estimated by COLMAP, without any specific compensation for motion blur or rolling shutter effects. This baseline serves as a reference point for evaluating the efficacy of our proposed motion blur compensation method.

**Rolling shutter pose optimization** As an alternative pose estimation method, we use our approach with both pose optimization and rolling-shutter compensation enabled, using the *factory intrinsics* and rolling shutter readout time reported by the mobile devices. The reasoning behind this is that COLMAP may use the camera intrinsics to compensate also for the rolling shutter effect when used with non-still images. Similarly, COLMAP-estimated poses do not generally represent the best solution for a given (different) set of camera intrin-

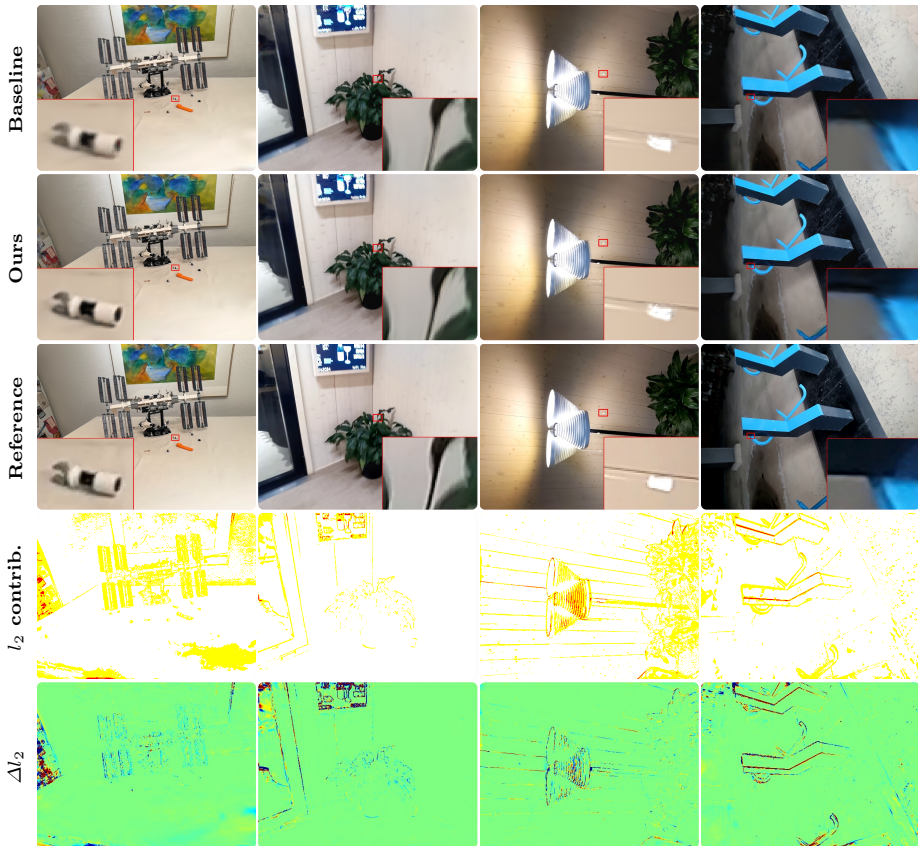


**Fig. 5:** Additional smartphone data reconstructions as in Fig. 4 for the scenes *lego2* (iPhone), *plant* (Pixel), *lamp* (Pixel), *bikerack* (S20).

sics, since slightly inaccurate intrinsics may be compensated by adjusting the poses. Hence enabling rolling-shutter compensation with COLMAP-estimated poses is not a good approach. We performed the experiments using both manual calibration data as well as the built-in calibration information from the devices.

**Two-pass pose optimization** When optimizing the poses, it is also necessary to change adjust the poses of the evaluation images. To this end, mostly due to ease of implementation, we choose an approach where we first train the model with pose optimization using all images. We then store the adjusted poses, and then train the model again without the evaluation images, but with fixed poses. An alternative would be to train with pose optimization with training images only and then optimize the poses of the evaluation images to minimize the loss on the 3DGS model, which is not modified during this optimization.

**Results** The real data results are given in Table 2 and visualized in Figs. 4 and 5. The pose-optimized version uses the manual calibration data. The corre-

**Table 3:** Real data timing results. Training wall clock time  $T$  (minutes) with and without motion blur compensation.

	$N_{\text{train}}$	RESOLUTION	BASELINE	MOTION BLUR
			$T$	$T$
IPHONE-LEGO1	21	1920×1440	20	59
IPHONE-LEGO2	23	1920×1440	20	91
IPHONE-LEGO3	21	1920×1440	45	67
IPHONE-POTS1	25	1920×1440	16	71
IPHONE-POTS2	26	1920×1440	18	50
PIXEL5-LAMP	35	1600×1200	13	65
PIXEL5-PLANT	30	1600×1200	12	44
PIXEL5-TABLE	23	1600×1200	31	37
S20-BIKE	43	1920×1440	17	51
S20-BIKERACK	32	1920×1440	18	60
S20-SIGN	28	1920×1440	20	105
AVERAGE			21	64

sponding results for the built-in calibration were similar, but slightly worse on the average, see App. D for details.

The motion blur compensation consistently improves the results over the COLMAP baseline, in terms of the PSNR, SSIM and LPIPS metrics, as well as in qualitative evaluation. The effect of the rolling-shutter pose optimization (with non-optimized intrinsics) are mixed. In the Android test sequences, the metrics are clearly and consistently improved, while in the iOS test, they are degraded.

We suspect the main reason for this is the strength of the rolling shutter effect. The tested Android devices have long read-out times,  $T_{\text{ro}} = 32.3$  ms and  $T_{\text{ro}} = 28.87$  ms for Pixel 5 and S20, respectively. The readout time of iPhone 15 is approximately 5 ms. The 3DGS pose optimization may be less robust than COLMAP and might more easily converge to wrong local minima. However, in the case of a strong rolling shutter effect, the modeling error from assuming a global shutter is large and COLMAP’s results are easier to improve.

Qualitatively, the sharpness of the reconstructions is subtly, but noticeably increased when motion blur compensation is enabled, as demonstrated in the highlighted details in Figs. 4 and 5. The versions with and without rolling shutter compensation did not show significant differences (*cf.* App. D). In cases where rolling shutter compensation and pose optimization improved results over the purely motion-blur-compensated case, the improved metrics are mostly explained by more consistent overall shape of the reconstruction, when three-dimensional rolling shutter warping is more accurately modelled.

The automatic selection of key frames for evaluation also played a significant role in our analysis, particularly in highlighting areas poorly represented in the training data. These areas, especially near the edges of the visual field, were more susceptible to artefacts that disproportionately affected the PSNR metric, underlining the challenges in balancing motion blur compensation with the preservation of image quality across the entire scene. These effects are visible near the edges of the error metric figures in Figs. 4 and 5.

**Timing tests** Our results were computed on NVidia A100 GPUs. The training times corresponding to the COLMAP baseline with and without blur are shown in Table 3. The increase in training times (here shown for a single test run) varies significantly by case. On the average, the motion-blur compensated version with  $N_{\text{blur}} = 5$  samples is approximately three times slower than the baseline, which is clearly faster than a 5-fold increase that could be expected in a simpler implementation. However, we note that our CUDA implementation was not yet profiled for new bottlenecks, and could have significant potential for further speed improvement. The memory consumption of our approach is not significantly higher than for the baseline Splatfacto model. For development purposes, we also successfully trained on consumer grade GPUs, such as NVidia RTX 4060 TI with 16 GB of VRAM.

## 5 Discussion and Conclusion

We demonstrated how blurring and rolling shutter effects can be efficiently implemented in the Gaussian Splatting (3DGS) framework. We quantitatively and qualitatively demonstrated that the method improves over the 3DGS Splatfacto baseline in both synthetic and real data experiments.

Similar to [18, 25], a relevant additional comparison would be testing against an implementation where training images would be first pre-processed with a deblurring or rolling-shutter unrolling method. However, this paper focused on demonstrating the feasibility of a simpler approach, where the blurring and rolling-shutter effects are directly incorporated into the differentiable 3D implicit representation.

Incorporating learning-based aspects directly into the 3D model generation instead of the 2D input data is a new and promising approach studied in, *e.g.*, [42, 43]. We believe that, in the context of differentiable rendering and 3D reconstruction, this approach is likely to prove superior to learning-based image manipulation as a pre-processing step.

The performance of our approach compared to purely image-based SoTA such as [25, 41] should be analyzed in more detail in follow-up work. Refining VIO-based velocity estimates in 3DGS (or NeRF) during training could also potentially improve reconstruction results. In addition, modelling local linear trajectories with more complex spline-based shapes as in [18, 41] could be an additional follow up work.

Data capture in-the-wild is typically done on smart phones with a rolling shutter sensor and during relative motion. These effects are rarely represented well in modern benchmark data for inverse rendering, limiting the real-world use of 3DGS based methods. Our work represents a significant step forward in the integration of motion blur and rolling shutter corrections within the 3DGS framework, opening up new avenues for research and application in differentiable rendering and 3D scene reconstruction.

The source code of our implementation is available at <https://github.com/SpectacularAI/3dgs-deblur>.

# Bibliography

- [1] Spectacular AI mapping tools (2024), <https://spectacularai.github.io/docs/sdk/tools/nerf.html>, accessed: 2024-03-01
- [2] Cai, J.F., Ji, H., Liu, C., Shen, Z.: Blind motion deblurring from a single image using sparse approximation. In: IEEE Conference on Computer Vision and Pattern Recognition (CVPR). pp. 104–111. IEEE (2009)
- [3] Chakrabarti, A.: A neural approach to blind motion deblurring. In: Leibe, B., Matas, J., Sebe, N., Welling, M. (eds.) European Conference on Computer Vision (ECCV). pp. 221–235. Cham (2016)
- [4] Community, B.O.: Blender – a 3D modelling and rendering package. Blender Foundation, Stichting Blender Foundation, Amsterdam (2018), <http://www.blender.org>
- [5] Dai, P., Zhang, Y., Yu, X., Lyu, X., Qi, X.: Hybrid neural rendering for large-scale scenes with motion blur. In: IEEE/CVF Conference on Computer Vision and Pattern Recognition (CVPR). pp. 154–164. IEEE Computer Society, Los Alamitos, CA, USA (2023)
- [6] Fan, B., Dai, Y., Zhang, Z., Liu, Q., He, M.: Context-aware video reconstruction for rolling shutter cameras. In: IEEE/CVF Conference on Computer Vision and Pattern Recognition (CVPR). pp. 17551–17561 (2022)
- [7] Fu, Y., Liu, S., Kulkarni, A., Kautz, J., Efros, A.A., Wang, X.: COLMAP-Free 3D Gaussian splatting. arXiv preprint arXiv:2312.07504 (2023)
- [8] Gong, D., Yang, J., Liu, L., Zhang, Y., Reid, I., Shen, C., van den Hengel, A., Shi, Q.: From motion blur to motion flow: A deep learning solution for removing heterogeneous motion blur. In: IEEE Conference on Computer Vision and Pattern Recognition (CVPR) (2017)
- [9] Grundmann, M., Kwatra, V., Castro, D., Essa, I.: Calibration-free rolling shutter removal. In: IEEE International Conference on Computational Photography (ICCP). pp. 1–8 (2012)
- [10] Hedborg, J., Forsén, P.E., Felsberg, M., Ringaby, E.: Rolling shutter bundle adjustment. In: IEEE Conference on Computer Vision and Pattern Recognition (CVPR). pp. 1434–1441 (2012)
- [11] Kaipio, J., Somersalo, E.: Statistical and computational inverse problems. Springer (2004)
- [12] Keetha, N., Karhade, J., Jatavallabhula, K.M., Yang, G., Scherer, S., Ramanan, D., Luiten, J.: SplatTAM: Splat, Track & Map 3D Gaussians for dense RGB-D SLAM. arXiv (2023)
- [13] Kerbl, B., Kopanas, G., Leimkühler, T., Drettakis, G.: 3D Gaussian Splatting for real-time radiance field rendering. ACM Transactions on Graphics (TOG) **42**(4) (2023)
- [14] Kim, H., Song, M., Lee, D., Kim, P.: Visual-inertial odometry priors for bundle-adjusting neural radiance fields. In: 2022 22nd International Conference on Control, Automation and Systems (ICCAS). pp. 1131–1136 (2022)

- [15] Kupyn, O., Budzan, V., Mykhailych, M., Mishkin, D., Matas, J.: DeblurGAN: Blind motion deblurring using conditional adversarial networks (2018)
- [16] Lao, Y., Ait-Aider, O.: A robust method for strong rolling shutter effects correction using lines with automatic feature selection. In: IEEE Conference on Computer Vision and Pattern Recognition (CVPR). pp. 4795–4803 (2018)
- [17] Lee, B., Lee, H., Sun, X., Ali, U., Park, E.: Deblurring 3D Gaussian Splatting (2024)
- [18] Li, M., Wang, P., Zhao, L., Liao, B., Liu, P.: USB-neRF: Unrolling shutter bundle adjusted neural radiance fields. In: International Conference on Learning Representations (ICLR) (2024)
- [19] Liang, C.K., Chang, L.W., Chen, H.H.: Analysis and compensation of rolling shutter effect. *IEEE Transactions on Image Processing* **17**(8), 1323–1330 (2008)
- [20] Liao, B., Qu, D., Xue, Y., Zhang, H., Lao, Y.: Revisiting rolling shutter bundle adjustment: Toward accurate and fast solution. In: IEEE/CVF Conference on Computer Vision and Pattern Recognition (CVPR). pp. 4863–4871 (2023)
- [21] Lin, C.H., Ma, W.C., Torralba, A., Lucey, S.: BARF: Bundle-adjusting neural radiance fields. *IEEE/CVF International Conference on Computer Vision (ICCV)* pp. 5721–5731 (2021)
- [22] Liu, P., Cui, Z., Larsson, V., Pollefeys, M.: Deep shutter unrolling network. In: IEEE/CVF Conference on Computer Vision and Pattern Recognition (CVPR). pp. 5940–5948 (2020)
- [23] Lovegrove, S., Patron-Perez, A., Sibley, G.: Spline fusion: A continuous-time representation for visual-inertial fusion with application to rolling shutter cameras. In: Proceedings of the British Machine Vision Conference (BMVC). pp. 93.1–93.11 (01 2013)
- [24] Lowe, D.G.: Distinctive image features from scale-invariant keypoints. *International Journal of Computer Vision* **60**(2), 91–110 (2004)
- [25] Ma, L., Li, X., Liao, J., Zhang, Q., Wang, X., Wang, J., Sander, P.V.: Deblur-NeRF: Neural radiance fields from blurry images. In: IEEE/CVF Conference on Computer Vision and Pattern Recognition (CVPR). pp. 12861–12870 (2022)
- [26] Matsuki, H., Murai, R., Kelly, P.H.J., Davison, A.J.: Gaussian splatting SLAM (2023)
- [27] Mildenhall, B., Srinivasan, P.P., Tancik, M., Barron, J.T., Ramamoorthi, R., Ng, R.: NeRF: Representing scenes as neural radiance fields for view synthesis. In: European Conference on Computer Vision (ECCV). Springer (2020)
- [28] Mohan M.R., M., Rajagopalan, A., Seetharaman, G.: Going unconstrained with rolling shutter deblurring. In: IEEE International Conference on Computer Vision (ICCV). pp. 4030–4038 (2017)
- [29] Park, K., Henzler, P., Mildenhall, B., Barron, J.T., Martin-Brualla, R.: CamP: Camera preconditioning for neural radiance fields. *ACM Transactions on Graphics (TOG)* (2023)



- [30] Rengarajan, V., Rajagopalan, A.N., Aravind, R.: From bows to arrows: Rolling shutter rectification of urban scenes. In: IEEE Conference on Computer Vision and Pattern Recognition (CVPR). pp. 2773–2781 (2016)
- [31] Schölkopf, B., Platt, J., Hofmann, T.: Blind motion deblurring using image statistics. In: Advances in Neural Information Processing Systems 19. pp. 841–848 (2007)
- [32] Schönberger, J.L., Frahm, J.M.: Structure-from-motion revisited. In: IEEE Conference on Computer Vision and Pattern Recognition (CVPR) (2016)
- [33] Schubert, D., Demmel, N., von Stumberg, L., Usenko, V., Cremers, D.: Rolling-shutter modelling for visual-inertial odometry. In: International Conference on Intelligent Robots and Systems (IROS) (2019)
- [34] Seiskari, O., Rantalankila, P., Kannala, J., Ylilammi, J., Rahtu, E., Solin, A.: HybVIO: Pushing the limits of real-time visual-inertial odometry. In: IEEE/CVF Winter Conference on Applications of Computer Vision (WACV). pp. 287–296. IEEE Winter Conference on Applications of Computer Vision, IEEE (2022)
- [35] Shan, Q., Jia, J., Agarwala, A.: High-quality motion deblurring from a single image. ACM Transactions on Graphics (TOG) **27**(3), 1–10 (2008)
- [36] Su, S., Heidrich, W.: Rolling shutter motion deblurring. In: IEEE Conference on Computer Vision and Pattern Recognition (CVPR). pp. 1529–1537 (2015)
- [37] Tai, Y.W., Brown, M.: Richardson–Lucy deblurring for scenes under a projective motion path. IEEE Transactions on Pattern Analysis and Machine Intelligence **33**, 1603–1618 (09 2011)
- [38] Tai, Y.W., Tan, P., Brown, M.S.: Richardson-lucy deblurring for scenes under a projective motion path. IEEE Transactions on Pattern Analysis and Machine Intelligence **33**(8), 1603–1618 (2011)
- [39] Tancik, M., Weber, E., Ng, E., Li, R., Yi, B., Kerr, J., Wang, T., Kristoffersen, A., Austin, J., Salahi, K., Ahuja, A., McAllister, D., Kanazawa, A.: Nerfstudio: A modular framework for neural radiance field development. In: ACM SIGGRAPH 2023 Conference Proceedings. SIGGRAPH ’23 (2023)
- [40] Vasu, S., Mohan M.R., M., Rajagopalan, A.: Occlusion-aware rolling shutter rectification of 3D scenes. In: IEEE/CVF Conference on Computer Vision and Pattern Recognition (CVPR). pp. 636–645 (2018)
- [41] Wang, P., Zhao, L., Ma, R., Liu, P.: BAD-NeRF: Bundle adjusted deblur neural radiance fields. In: IEEE/CVF Conference on Computer Vision and Pattern Recognition (CVPR). pp. 4170–4179 (June 2023)
- [42] Weber, E., Holynski, A., Jampani, V., Saxena, S., Snively, N., Kar, A., Kanazawa, A.: NeRFfiller: Completing scenes via generative 3D inpainting. In: IEEE/CVF Conference on Computer Vision and Pattern Recognition (CVPR) (2024)
- [43] Wu, R., Mildenhall, B., Henzler, P., Park, K., Gao, R., Watson, D., Srinivasan, P.P., Verbin, D., Barron, J.T., Poole, B., Holynski, A.: ReconFusion: 3D reconstruction with diffusion priors. arXiv preprint arXiv:2312.02981 (2023)

- [44] Xu, L., Jia, J.: Two-phase kernel estimation for robust motion deblurring. In: European Conference on Computer Vision (ECCV). pp. 157–170. Springer (2010)
- [45] Yan, C., Qu, D., Wang, D., Xu, D., Wang, Z., Zhao, B., Li, X.: GS-SLAM: Dense visual SLAM with 3D Gaussian Splatting (2024)
- [46] Ye, V., Kanazawa, A.: Mathematical supplement for the `gsplat` library (2023)
- [47] Ye, V., Turkulainen, M., the Nerfstudio team: `gsplat`, <https://github.com/nerfstudio-project/gspat>
- [48] Zamir, S.W., Arora, A., Khan, S., Hayat, M., Khan, F.S., Yang, M.H., Shao, L.: Multi-stage progressive image restoration. In: IEEE/CVF Conference on Computer Vision and Pattern Recognition (CVPR). pp. 14816–14826 (2021)

## A Method Details

### A.1 Gaussian parametrization

In `gsplat`, the Gaussian covariances  $\Sigma$  in world coordinates are parametrized as

$$\Sigma = R(q) \text{diag}(\text{sigmoid}(s_1, s_2, s_3)) R(q)^\top \quad (11)$$

where  $q \in \mathbb{R}^4$  is a normalized quaternion corresponding to a rotation matrix  $R(q) \in \text{SO}(3)$  and  $(s_1, s_2, s_3) \in \mathbb{R}$  are scale parameters. This is not changed in our implementation, but we use  $\Sigma$  instead of the above parameters in this paper for brevity and clarity.

### A.2 Transforming Gaussians from world to pixel coordinates

In 3DGS, the rendering equation can be written as,

$$C_i(x, y, P, \mathcal{G}) = r(x, y, \pi(\hat{p}(\mathcal{G}, P))) \quad (12)$$

where  $\hat{p} : (\mu, \Sigma, \theta, P) \mapsto (\hat{\mu}, \hat{\Sigma}, c)$  maps each (visible) Gaussian from the world coordinate system to the *camera coordinate* system

$$\hat{\mu}_{i,j} = R_i^\top (\mu_j - p_i), \quad \hat{\Sigma}_{i,j} = R_i^\top \Sigma_j R_i, \quad c_{i,j} = \theta_j \left( \frac{\mu_j - p_i}{\|\mu_j - p_i\|} \right) \quad (13)$$

where the colour  $c$  is computed by evaluation the spherical harmonic function at the normalized viewing direction. We use spherical harmonics of degree three. The function  $\pi : (\hat{\mu}, \hat{\Sigma}) \mapsto (\mu', d, \Sigma')$  projects Gaussians from camera coordinates to pixel coordinates with depth:

$$d = \tilde{\mu}_z, \quad \mu' = (\tilde{\mu}_x/d, \tilde{\mu}_y/d), \quad \Sigma' = J_i \hat{\Sigma} J_i^\top, \quad (14)$$

where  $\tilde{\mu} = K_i \hat{\mu}$  and  $J_i$  is the Jacobian matrix of the pinhole camera projection  $\hat{\mu} \mapsto \mu'$  with intrinsic camera matrix  $K_i$ :

$$J_i = \begin{bmatrix} f_x & 0 & 0 \\ 0 & f_y & 0 \end{bmatrix}, \quad K_i = \begin{bmatrix} f_x & 0 & c_x \\ 0 & f_y & c_y \\ 0 & 0 & 1 \end{bmatrix}. \quad (15)$$

Note that unlike the original `gsplat` [46] and the Inria implementations, we do not use the OpenGL NDC coordinate system as an intermediate step between projecting Gaussians to pixel coordinates.

The Gaussian with low depth  $d < d_{\min}$  or pixel coordinates  $(\mu'_x, \mu'_y)$  too far outside the image boundaries  $[0, W) \times [0, H)$  are discarded in the next rendering phases represented by the function  $r$ .

### A.3 Differentiation with respect to the camera pose

We seek to differentiate the rendering equation Eq. (12) with respect to the current camera pose parameters  $P_i \in \text{SE}(3)$ . The key to camera pose optimization is differentiating the intermediate projection terms Eq. (13) with respect to some parametrization of  $P_i = [R_i | p_i]$ . First, note that the Jacobian<sup>1</sup> of the Gaussian mean in camera coordinates with respect to the camera center  $p_i$  is

$$\frac{\partial \hat{\mu}_{i,j}}{\partial p_i} = -R_i^\top = -\frac{\partial \hat{\mu}_{i,j}}{\partial \mu_j} \quad (16)$$

and if we neglect the effect of  $p_i$  on  $c_{i,j}$ , *i.e.*, the view-dependency of the colors, and on the covariances  $\hat{\Sigma}_{i,j}$ , we can approximate:

$$\begin{aligned} \frac{\partial C_i}{\partial p_i} &= \sum_j \left( \frac{\partial C_i}{\partial \hat{\mu}_{i,j}} \frac{\partial \hat{\mu}_{i,j}}{\partial p_i} + \frac{\partial C_i}{\partial \hat{\Sigma}_{i,j}} \frac{\partial \hat{\Sigma}_{i,j}}{\partial p_i} + \frac{\partial C_i}{\partial c_{i,j}} \frac{\partial c_{i,j}}{\partial p_i} \right) \\ &\approx \sum_j \frac{\partial C_i}{\partial \hat{\mu}_{i,j}} \frac{\partial \hat{\mu}_{i,j}}{\partial p_i} = - \sum_j \frac{\partial C_i}{\partial \hat{\mu}_{i,j}} \frac{\partial \hat{\mu}_{i,j}}{\mu_j} \approx - \sum_j \frac{\partial C_i}{\partial \mu_j}, \end{aligned}$$

that is, moving the camera to direction  $\Delta p$  is approximately the same as moving all the visible Gaussians to the opposite direction  $-\Delta p$ .

Furthermore, using Eq. (16) and ignoring effects on color-dependency, we can use the following expression

$$\frac{\partial C_i}{\partial \mu_j} = \frac{\partial C_i}{\partial \hat{\mu}_{i,j}} \frac{\partial \hat{\mu}_{i,j}}{\partial \mu_j} + \frac{\partial C_i}{\partial c_{i,j}} \frac{\partial c_{i,j}}{\partial \mu_j} \approx \frac{\partial C_i}{\partial \hat{\mu}_{i,j}} \frac{\partial \hat{\mu}_{i,j}}{\partial \mu_j} = \frac{\partial C_i}{\partial \hat{\mu}_{i,j}} R_i^\top \quad (17)$$

The derivative of the rendering equation with respect to the rotation of the camera pose can also be expressed by neglecting the effect of small rotations on the shape of  $\hat{\Sigma}_{i,j}$  of the Gaussians in camera coordinates. The derivative of the pixel colour  $C_i$  with respect to any rotation matrix  $R_i$  component  $\nu$  becomes

$$\begin{aligned} \frac{\partial C_i}{\partial \nu} &\approx \sum_j \frac{\partial C_i}{\partial \hat{\mu}_{i,j}} \frac{\partial \hat{\mu}_{i,j}}{\partial \nu} \approx \sum_j \frac{\partial C_i}{\partial \mu_j} R_i \frac{\partial \hat{\mu}_{i,j}}{\partial \nu} = \sum_j \frac{\partial C_i}{\partial \mu_j} R_i \left( \frac{\partial R_i}{\partial \nu} \right)^\top (\mu_j - p_i) \\ &= \sum_j \frac{\partial C_i}{\partial \mu_j} R_i \left( \frac{\partial R_i}{\partial \nu} \right)^\top R_i \hat{\mu}_{i,j} = - \sum_j \frac{\partial C_i}{\partial \mu_j} \frac{\partial R_i}{\partial \nu} \hat{\mu}_{i,j} \end{aligned}$$

The benefit of this approach is that derivatives with respect to both rotation  $R_i$  and translation  $p_i$  of the camera can be approximated in terms of the derivatives  $\frac{\partial C_i}{\partial \mu_j}$  with respect to the Gaussian means, and other properties that are readily available in the 3DGS backwards pass.

<sup>1</sup> Slight abuse of notation: we use  $\frac{\partial}{\partial \nu}$  notation for all derivatives, including Jacobian matrices and multi-dimensional tensors, such as  $\frac{\partial \hat{\Sigma}_{i,j}}{\partial p_i}$

The above formulas hold for camera-to-world transformations  $P = [R|p]$ . For their world-to-camera counterparts  $P' = [R'|p'] = [R'^\top | -R'^\top p]$ , we can first change Eq. (13) to  $\hat{\mu}_{i,j} = R'_i \mu_j + p'$  and then write

$$\frac{\partial C_i}{\partial \mu_j} \approx \frac{\partial C_i}{\partial \hat{\mu}_{i,j}} \frac{\partial \hat{\mu}_{i,j}}{\partial \mu_j} = \frac{\partial C_i}{\partial \hat{\mu}_{i,j}} R'_i, \quad \frac{\partial \hat{\mu}_{i,j}}{\partial p'_i} = I = R'_i (R'_i)^\top = \frac{\partial \hat{\mu}_{i,j}}{\partial \mu_j} (R'_i)^\top \quad (18)$$

and, consequently

$$\frac{\partial C_i}{\partial p_i} \approx \sum_j \frac{\partial C_i}{\partial \hat{\mu}_{i,j}} \frac{\partial \hat{\mu}_{i,j}}{\partial p'_i} = \sum_j \frac{\partial C_i}{\partial \hat{\mu}_{i,j}} \frac{\partial \hat{\mu}_{i,j}}{\partial \mu_j} (R'_i)^\top \approx \sum_j \frac{\partial C_i}{\partial \mu_j} (R'_i)^\top \quad (19)$$

and

$$\frac{\partial C_i}{\partial \nu} \approx \sum_j \frac{\partial C_i}{\partial \mu_j} (R'_i)^\top \frac{\partial R'_i}{\partial \nu} \mu_j. \quad (20)$$

The latter format in Eq. (19) and Eq. (20) is used in our implementation.

#### A.4 Derivation of the pixel velocity formula

The derivative of the pixel coordinates  $\mu'$  of a Gaussian center with respect to camera motion  $P(t)$  is

$$\begin{aligned} \frac{d}{dt} \mu'(P(t)) &= J_{\hat{\mu} \rightarrow \mu', t} \frac{d}{dt} \hat{\mu}(P(t)) \\ &= J_i \frac{d}{dt} R_i^\top(t) (\mu_j - p_i(t)) \\ &= J_i \frac{d}{dt} (R_i \exp(t[\omega_j]_\times))^\top (\mu_j - (p_i + t \cdot R_i v_i)) \\ &= J_i ([[\omega_j]_\times^\top \exp(t[\omega_j]_\times)^\top R_i^\top] (\mu_j - p_i(t)) - \exp(t[\omega_j]_\times)^\top R_i^\top (R_i v_i)) \\ &= J_i ([[\omega_j]_\times^\top \exp(t[\omega_j]_\times)^\top \hat{\mu}_{i,j} - \exp(t[\omega_j]_\times)^\top v_i]. \end{aligned}$$

The derivative at  $t = 0$  is

$$\frac{d}{dt} \mu'(P(t))|_{t=0} = J_i ([[\omega_j]_\times^\top \hat{\mu}_{i,j} - v_i] = -J_i (\omega_j \times \hat{\mu}_{i,j} + v_i) = v'_{i,j}.$$

#### A.5 Key Frame Selection

The level of motion blur in a given frame can be estimated using a VIO or VISLAM system by examining the pixel velocities of the 3D positions  $l_j$ ,  $j = 1, \dots, N_i^{\text{lm}}$  of the sparse SLAM landmarks visible in the frame in question. The Open Source part of the Spectacular AI Mapping tools [1] computes a *motion blur score* as

$$M_i = \frac{1}{N_i^{\text{lm}}} \sum_j \|J_i (\omega_i \times (R_i l_j + p_i) + v_i)\| \quad (21)$$

where  $J_i$  is as in Eq. (15),  $(R_i, t_i)$  is the world-to-camera pose and  $(v_i, \omega_i)$  are the instantaneous camera-coordinate linear and angular velocities of the frame, respectively.

To reduce sporadic motion blur, the Spectacular AI software drops all key frame candidates  $i$  which have the highest blur score in a neighbourhood of 4 key frame candidates  $([i - 2, i - 1, i, i + 1])$ . We utilize the motion blur score computed using Eq. (21) also for the training and evaluation subset partitions described in Sec. 4.2.

Additionally, we ran an experiment where the evaluation frames were picked by selecting every 8th key frame and switched off the motion blur score based filtering. See Table 5. The numeric results were very similar with motion blur filtering enabled. In the main paper, we chose to include the results with motion blur filtering enabled, to demonstrate that our approach can decrease motion-blur-induced effects even after the easy options for filtering blurry input frames have been exhausted. This highlights the usefulness of deblurring utilizing a 3D image formation model in the context of differentiable rendering.

## A.6 Transferring velocities from one SLAM method to another

Assuming we have a matching set of  $N$  poses  $P_i = (R_i, p_i)$  for two methods (COLMAP and SAI), which differ by a Sim(3) transformation, we can map the linear frame velocities as

$$v_i = \frac{s(p^{\text{COLMAP}})}{s(p^{\text{SAI}})} v_i^{\text{SAI}}, \quad s^2(p) := \sum_i \left\| p_i - \frac{\sum_i p_i}{N} \right\|^2. \quad (22)$$

Note that the result does not depend on the rotation or translation part of the transformation and the accuracy of the result depends on the average scale consistency of each method.

## B Data Sets and Metrics

### B.1 Modifications to the Deblur-NeRF data set

The original version of the Deblur-NeRF data set [25] did not include the velocity data, which was randomly generated by the original authors with an unspecified seed number. We regenerated the images using the Blender [4] files, which we modified by fixing the random seed, and also included velocity information in our outputs. All of the models mentioned in the [25] were also not available (*e.g.* ‘trolley’), and those cases are omitted from our version of the data set.

Furthermore, we switched from the custom 10-sample blur implementation to Blender’s built-in motion blur and rolling-shutter effects, which are less prone to sampling artefacts. Finally we adjusted the caustics rendering settings in the Blender scenes to reduce non-deterministic raytracing sampling noise in the data with reasonable sample counts. As a result, our modified data set, published as

supplementary material, provides effectively deterministic rendering capabilities and improves the reproducibility of the results compared to the original version.

The modified data set also includes de-focus blur, which was studied in [25] but not in this paper, which is why this variation is also omitted from Table 1.

## C Experiment Details

**Splatfacto hyperparameters** . The following hyperparameters were tuned in the Splatfacto baseline method to improve obvious issues related to its performance on our datasets: *(i)* For the synthetic data, we limit the training iteration count to 15k, instead of the default, 30k, to avoid gap-like artefacts that started to appear at higher iteration counts. *(ii)* For the smartphone data, the iteration count was limited to 20k for the same reason. *(iii)* The minimum RGB level of all color channels was set to 10 in the training data, to avoid large negative logit color values, which resulted in artefacts in the proximity of dark areas in certain scenes.

The same hyperparameters and modifications were also used for our motion-blur and rolling shutter compensated methods.

## D Additional Results

### D.1 Synthetic data

The synthetic data results for the remaining scenes are visualized in Fig. 6 and Fig. 7.

### D.2 Smartphone data

The accuracy of the method with manual camera calibration is compared to the built-in calibration values reported by the devices in Table 4, which also includes the results for a method variant where rolling shutter compensation was used without motion blur compensation.

Table 5 shows the results for an experiment where all motion-blur-based scoring for training-evaluation split and key frame selection have been disabled. The results are relatively similar to those in Table 2. However, with more blurry evaluation frames, it becomes less clear if the metrics reward sharp reconstructions or accurate simulation of motion blur and rolling shutter effects in the forward model.

A qualitative evaluation of de-blurring with and without rolling shutter compensation is presented in Fig. 8. In both method variants, the details are sharpened in comparison to the baseline.

Finally, the reconstructions for the remaining smartphone datasets presented in Table 2 are shown in Fig. 9.

**Table 4:** Additional results in the rolling-shutter pose optimization mode: Rolling-shutter only (built-in calibration), and rolling shutter + motion blur compensation with built-in and manual calibration. The rightmost column matches that of Table 2.

	RS ONLY (BUILT-IN)			BUILT-IN CALIB.			MANUAL CALIB.		
	PSNR↑	SSIM↑	LPIPS↓	PSNR↑	SSIM↑	LPIPS↓	PSNR↑	SSIM↑	LPIPS↓
IPHONE-LEGO1	26.40	.859	.193	26.37	<b>.871</b>	<b>.161</b>	<b>26.40</b>	.869	.164
IPHONE-LEGO2	26.41	.892	.153	<b>28.13</b>	<b>.907</b>	<b>.133</b>	24.73	.853	.195
IPHONE-LEGO3	23.96	.743	.275	<b>24.55</b>	<b>.765</b>	<b>.238</b>	22.93	.720	.282
IPHONE-POTS1	<b>27.66</b>	.864	.204	27.46	.871	.177	27.50	<b>.876</b>	<b>.169</b>
IPHONE-POTS2	25.45	.781	.317	25.83	.806	.255	<b>26.32</b>	<b>.821</b>	<b>.234</b>
PIXEL5-LAMP	28.66	.791	.315	28.11	.793	.293	<b>30.09</b>	<b>.820</b>	<b>.258</b>
PIXEL5-PLANT	26.68	.893	.302	26.77	.894	.275	<b>27.32</b>	<b>.908</b>	<b>.242</b>
PIXEL5-TABLE	29.55	.856	.341	29.91	.858	.312	<b>31.01</b>	<b>.884</b>	<b>.278</b>
S20-BIKE	27.45	.881	.304	27.92	.885	.298	<b>28.18</b>	<b>.894</b>	<b>.262</b>
S20-BIKERACK	25.72	.783	.342	25.71	.783	.343	<b>26.68</b>	<b>.797</b>	<b>.297</b>
S20-SIGN	24.20	.740	.293	24.68	.750	.292	<b>25.89</b>	<b>.780</b>	<b>.259</b>
AVERAGE	26.56	.826	.276	26.86	.835	.252	<b>27.00</b>	<b>.838</b>	<b>.240</b>

**Table 5:** Results corresponding to Table 2 with motion-blur-based key frame selection and training-evaluation split disabled. Built-in calibration used in *RS pose opt*

	COLMAP BASELINE			COLMAP + BLUR			RS POSE OPT + BLUR		
	PSNR↑	SSIM↑	LPIPS↓	PSNR↑	SSIM↑	LPIPS↓	PSNR↑	SSIM↑	LPIPS↓
IPHONE-LEGO1	26.68	.890	.200	<b>27.06</b>	<b>.910</b>	<b>.165</b>	26.75	.880	.181
IPHONE-LEGO2	27.15	.911	.153	28.01	<b>.925</b>	<b>.135</b>	<b>28.48</b>	.908	.138
IPHONE-LEGO3	22.92	.770	.334	<b>23.31</b>	<b>.815</b>	<b>.261</b>	22.62	.780	.281
IPHONE-POTS1	28.18	.912	.211	<b>28.76</b>	<b>.926</b>	<b>.173</b>	27.44	.898	.206
IPHONE-POTS2	28.30	.867	.292	28.63	<b>.881</b>	<b>.242</b>	<b>28.65</b>	.858	.268
PIXEL5-LAMP	27.85	.784	.377	27.81	.784	.347	<b>29.42</b>	<b>.796</b>	<b>.334</b>
PIXEL5-PLANT	26.68	.928	.227	26.95	<b>.933</b>	<b>.209</b>	<b>27.85</b>	.929	.239
PIXEL5-TABLE	28.82	.912	.281	29.34	<b>.922</b>	<b>.260</b>	<b>31.52</b>	.912	.293
S20-BIKE	26.49	.880	.293	27.64	.889	<b>.271</b>	<b>29.19</b>	<b>.892</b>	.301
S20-BIKERACK	25.99	.822	<b>.278</b>	<b>26.26</b>	<b>.822</b>	.286	25.33	.787	.367
S20-SIGN	22.70	.744	.304	23.89	.762	<b>.291</b>	<b>25.26</b>	<b>.766</b>	<b>.303</b>
AVERAGE	26.52	.856	.268	27.06	<b>.870</b>	<b>.240</b>	<b>27.50</b>	.855	.265

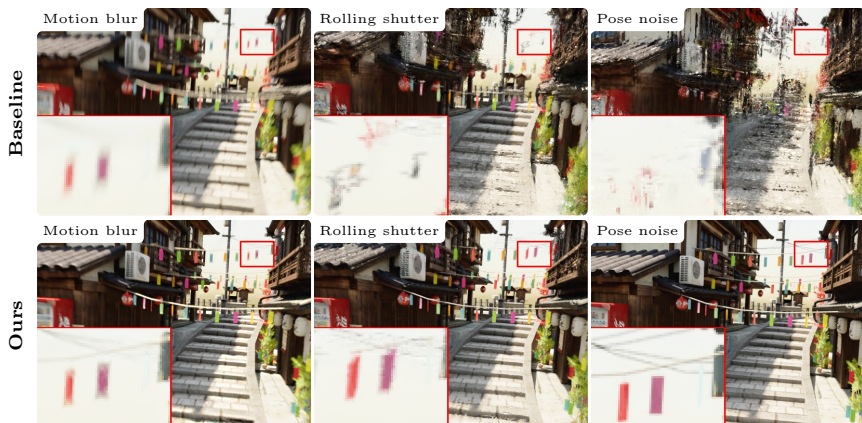


**Fig. 6:** 3DGS reconstructions from the synthetic tanabata scene



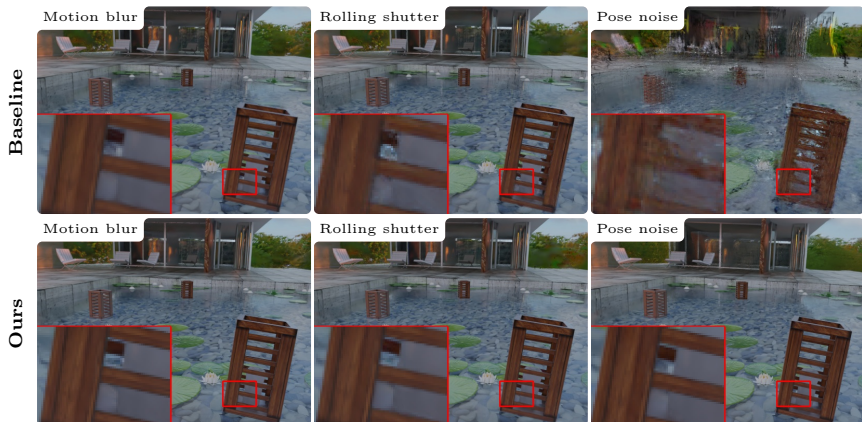


Fig. 7: 3DGS reconstructions from the synthetic pool scene

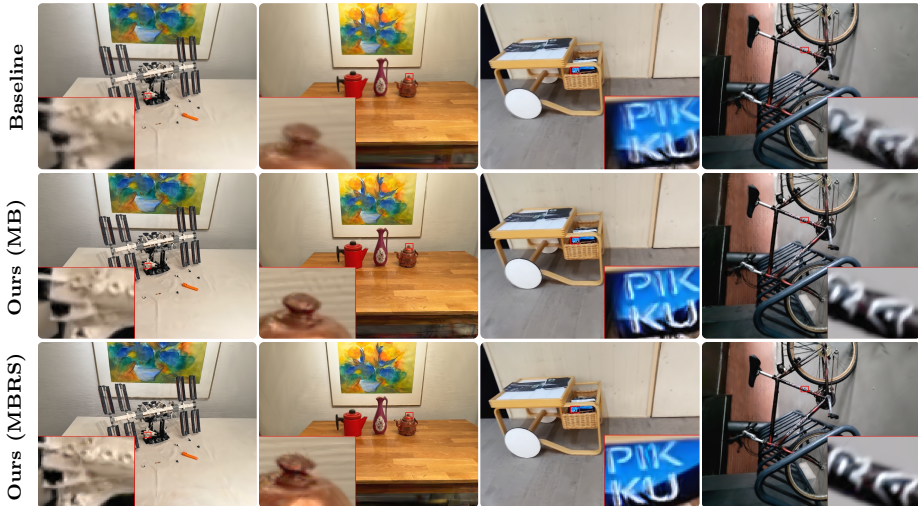
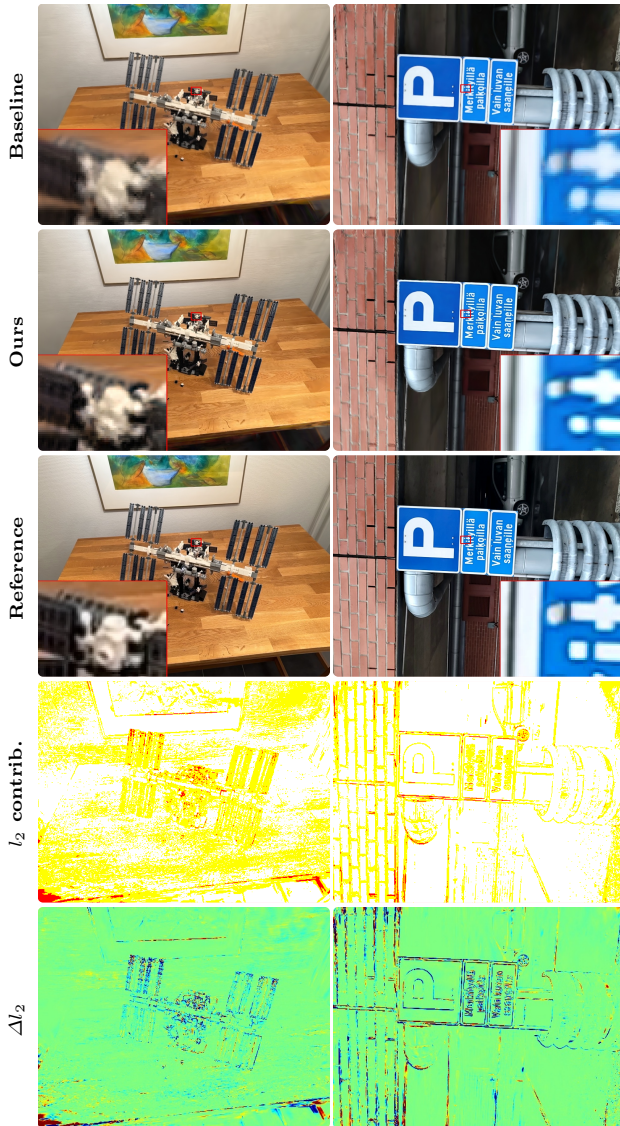


Fig. 8: Empirical ablations on deblurring with and without rolling shutter pose optimization on four real-world smartphone data scenes with rolling shutter effects. Our method with both motion blur and rolling shutter compensation (MBRS) gives sharper artefact-free reconstructions compared to just motion blur compensation (MB).



**Fig. 9:** Additional smartphone data reconstructions as in Fig. 4 for the scenes `lego3` (iPhone) and `sign` (S20).